ACS Energy LETTERS

http://pubs.acs.org/journal/aelccp

Improved Alkaline Hydrogen Oxidation on Strain-Modulated Pt Overlayers at Ordered Intermetallic Pt−Sb Cores

Tianyao Gong, Hamdan Alghamdi, David Raciti,* and Anthony Shoji Hall*

Cite This: *ACS Energy Lett.* 2023, 8, 685−690

Read Online

ACCESS | Metrics & More | Article Recommendations | Supporting Information

ABSTRACT: **The electro-oxidation of H_2 (HOR) is 200× slower in base than in acid, hampering the deployment of alkaline fuel cells. It is disputed whether the hydrogen binding energy (HBE) or a bifunctional effect is the primary contributor to the improved HOR performance of alloy materials, because these effects are difficult to disentangle. Here, we used ordered intermetallic compounds (OICs) to produce strain-modulated Pt shells, in which PtSb@Pt and $PtSb_2$@Pt exhibited compressive or tensile strain, respectively, to Pt. The HBE was tuned by the crystal structure of the OICs, allowing us to use the same two elements in the alloy and thus remove convolution from the bifunctional effect. PtSb@Pt exhibited a weaker HBE than Pt, achieving an exchange current density (j_o) 1.6× larger than Pt. However, $PtSb_2$@Pt exhibited a higher HBE, lowering the j_o value by 1.2× compared to Pt. This work demonstrated that high alkaline HOR activity can be achieved solely by tuning the HBE.**

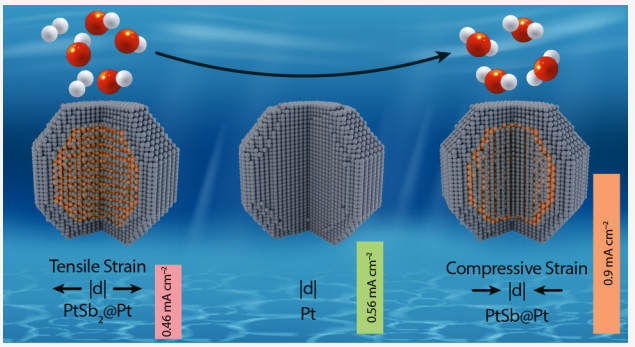

Alkaline exchange membrane fuel cells (AEMFCs) have emerged as an inexpensive and robust renewable energy conversion device that is capable of relaxing requirements of precious-metal catalysts at the cathode. However, the anode reaction, the hydrogen oxidation reaction (HOR), is 200× slower in alkaline environments in comparison to that in acidic environments.[1−4] Therefore, the opportunity for low-cost fuel cells is hindered by the high loading of Pt-group metals (PGM) required (>0.1 mg cm_{Pt}^{-2}) to mediate the alkaline HOR at reasonable reaction rates.[5] Improvements in PGM-based HOR catalysts are required for AEMFCs to be competitive with other energy generation devices.[1−3,5−7] If improved HOR catalysts are developed, then alkaline fuel cells with low loadings of precious metals can be realized.

Understanding the mechanism of the HOR under alkaline conditions is crucial to enable the development of high-performance catalysts. The mechanistic sequence for the HOR starts with the adsorption of H_2 and its subsequent conversion to a surface-adsorbed H-adatom (H_{ads}) by the Tafel or Heyrovsky step (eqs 1 and 2). The H_{ads} is then desorbed into solution to form H_2O under alkaline conditions (eq 3). In alkaline solutions the rate-determining step (RDS) for the HOR is thought to be the Volmer step or Heyrovsky step, both of which involve a reaction of H_2 or H_{ads} with OH^-.[1,2,8,9]

$$\text{Tafel step: } H_2 \rightarrow 2H_{ads} \quad (1)$$

$$\text{Heyrovsky step: } H_2 + OH^- \rightarrow H_2O + H_{ads} + e^- \quad (2)$$

$$\text{Volmer step: } H_{ads} + OH^- \rightarrow H_2O + e^- \quad (3)$$

Considerable progress has been made in enhancing the HOR kinetics by alloying Pt with a more oxophilic element such as Ni, Mo, Ru, Fe, Co, etc.[3,4,9−15] The complexity of alloy surfaces makes it difficult to determine if the enhancements are from changes in the hydrogen binding energy (HBE) and adsorbed OH (henceforth denoted as OH_{ads}) coverage on the Pt sites or from a bifunctional effect in which the H_{ads} on the Pt sites reacts with OH_{ads} on the more oxophilic solute atoms.[2,3,16] Several studies have shown that the presence of an oxophilic adatom on the surface of Pt has a potent effect on the HOR performance.[9,16,17] However, some studies have hypothesized that the HBE is the sole reason for the enhanced HOR performance of Pt alloys. This thought, however, may be

Received: November 1, 2022
Accepted: December 15, 2022
Published: December 22, 2022

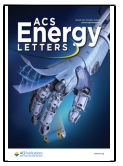

https://doi.org/10.1021/acsenergylett.2c02473
ACS Energy Lett. 2023, 8, 685−690

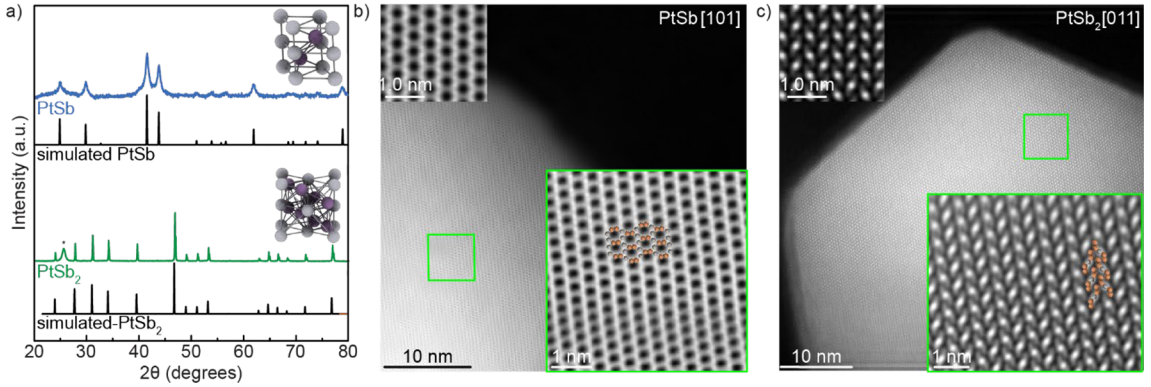

Figure 1. (a) Powder X-ray diffraction (XRD) of PtSb and $PtSb_2$ nanoparticles supported on carbon. The insets show the unit cells of ordered intermetallic $PtSb_2$ and PtSb. The simulated XRD patterns of PtSb and $PtSb_2$ are from ICSD collection codes No. 43105 and No. 16969, respectively. High-resolution HAADF-STEM images of freshly synthesized (b) PtSb and (c) $PtSb_2$ nanoparticles. The insets on the top left of (b) and (c) are simulated crystal lattices along the PtSb [101] and $PtSb_2$[011], respectively. The insets at the bottom right of (b) and (c) with green borders are enlarged regions of the green boxes of the TEM images. An overlay of the simulated crystal are shown in the enlargements of the crystal: the orange spheres depict Sb, and the gray spheres depict Pt.

an oversimplification, since electronic perturbations to Pt can alter the Pt−O adsorption energy—as has been well documented in catalyst design for the oxygen reduction reaction—as well as the HBE.[18,19] This is important because adsorbed OH^- has been shown to poison PGM surfaces during the ORR; therefore, it is not clear if adsorbed OH^- on Pt sites participates actively as per eqs 2 and 3 or is a poisoning species.[20] Therefore, how alloying changes the HBE and coverage of OH^- on Pt sites and its correlation to the HOR performance are poorly understood. A strategy for electronically perturbing surface Pt sites without convolution from different adatoms on the surface must be designed to understand the role of the HBE and adsorbed OH^- on Pt sites in the alkaline HOR. This can be accomplished by designing catalysts with Pt shells that exhibit tensile or compressive strain to tune the adsorption energy of reaction intermediates in opposite directions. However, this cannot be accomplished with solid-solution alloys, since these materials adopt the same crystal structure as the parent elements; thus, the strain field can only be moved in one direction (lower or higher, but not both, relative to Pt) since the lattice parameter—and therefore the *d* spacing—and composition are linked by Vegard's law.[21] This would necessitate the use of different alloying elements to make Pt-shell structures with controllable strain fields, but the presence of residual amounts of the alloying element, especially those with differing identity, can make it difficult to separate strain from the bifunctional effect. To address this issue, we propose to utilize ordered intermetallic compounds (OICs), alloys that possess long-range atomic ordering, as a platform for preparing strain-modulated catalysts to uncover detailed structure−property relationships in the HOR.[10,19,22−38]

Herein, we interrogated a series of ordered intermetallic Pt−Sb nanoparticles (PtSb and $PtSb_2$) for the alkaline HOR. Pt−Sb alloys have high melting points and thus evolve to self-passivating core@shell Pt−Sb@Pt under potential cycling.[38] The strained Pt layers on top of the ordered intermetallic Pt−Sb cores exhibit either compressive or tensile strain depending on the crystal structure of the core, therefore enabling weaker or strengthened adsorption energy of reaction intermediates relative to Pt. The use of the same alloying element to produce tensile or compressive strain on Pt eliminates convolution from the bifunctional effect caused by atoms with different identities, which may have drastically different oxophilicities, that might be present on the surface or be exposed through pinholes in the Pt shell. The Pt−Sb@Pt materials were found to exhibit exchange current densities 1.6× higher (PtSb@Pt) and 1.2× lower ($PtSb_2$@Pt) than those of benchmark Pt catalysts for compressively strained and tensile strained Pt overlayers, respectively. PtSb@Pt has among the highest activity for a PGM-based material for the alkaline HOR, exhibiting exchange current densities which match state-of-the art Pt−Ru alloys while containing 50% less precious metal (Table S1).[35] Not only does PtSb exhibit improved catalytic performance compared to conventional Pt catalysts but it is also lower in cost, since there is a 50% reduction in the amount of precious metals in the material, indicating that it is a viable candidate for AEMFC anodes.

Ordered intermetallic phases of Pt−Sb supported on carbon were prepared with a loading of 40 wt % (Pt basis) on carbon supports; more details can be found in the Supporting Information. The crystal structures of the resulting materials were probed by X-ray diffraction (XRD), showing that PtSb (space group $P6_3/mmc$, No. 194) and $PtSb_2$ (space group $Pa\bar{3}$, No. 205) were formed (Figure 1a). $PtSb_2$ showed a peak near 25° that corresponded to the (002) plane of the carbon support; this peak is marked with an asterisk. Inductively coupled plasma mass spectrometry (ICP-MS) was used to determine the composition of the materials. The atomic ratios (Pt:Sb) of PtSb and $PtSb_2$ were found to be 1:1 and 1:2.12, respectively. Transmission electron microscopy (TEM) was used to characterize the crystalline structure and estimate the particle size distribution of the carbon-supported ordered intermetallic Pt−Sb materials (Figures S1 and S2). TEM images showed that the Pt−Sb and commercial Pt benchmark catalysts uniformly coated the carbon support. The average particle sizes were found to be 4.4 ± 0.6 nm, 12.4 ± 2.6 nm, and 22.3 ± 4.2 nm for Pt, PtSb, and $PtSb_2$, respectively. High-angle annular dark field (HAADF) TEM images confirmed that as-synthesized PtSb and $PtSb_2$ exhibited atomic scale ordering (Figure 1b,c). Taken together, the data indicated that nominally pure phases of PtSb and $PtSb_2$ were formed.

The ordered intermetallic Pt−Sb materials and Pt were evaluated by cyclic voltammetry (CV) in N_2-saturated 0.1 mol

https://doi.org/10.1021/acsenergylett.2c02473
ACS Energy Lett. 2023, 8, 685−690

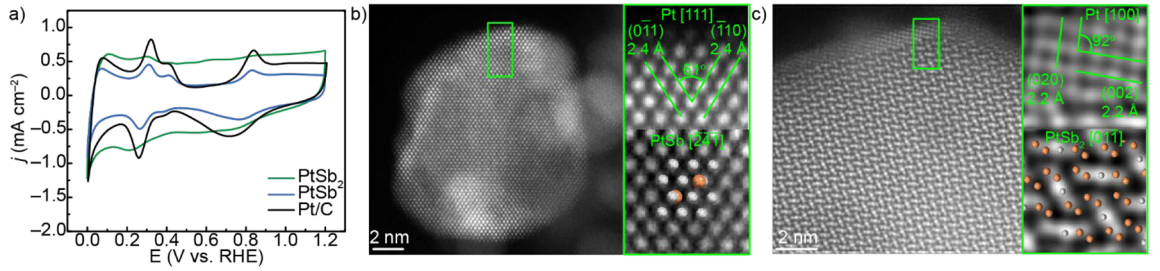

Figure 2. (a) Stabilized cyclic voltammograms (CVs) normalized by the geometric area. (b) STEM/HRTEM image for PtSb nanoparticles after cycling, showing that a PtSb@Pt structure has formed. (c) STEM/HRTEM image for $PtSb_2$ nanoparticles after cycling, showing that a $PtSb_2$@Pt structure has formed.

L^{-1} KOH between 0 to 1.2 V vs the reversible hydrogen electrode (RHE) to evaluate the surface redox features and dealloy Sb from the surface (Figure S3). As Sb is etched from the material the Pt adatoms diffuse and restructure to form a self-passivating compact Pt shell over the Pt−Sb cores. The formation of self-passivating noble-metal shells over noble-metal alloy cores by dealloying is commonly observed on alloy nanoparticles.[39−41] An overlay of the stabilized CVs of the Pt−Sb materials and Pt suggested that the surface of PtSb was similar to that of elemental Pt (Figure 2a). $PtSb_2$ displayed Pt-like features as well; however, the hydrogen underpotential deposition waves (0.2−0.5 V) and Pt oxidation/reduction waves (~0.6−1.0 V) were broadened relative to Pt and PtSb. The similarity between the CV profiles of Pt and those of the stabilized Pt−Sb intermetallic materials suggested that a Pt-rich shell had formed over the ordered intermetallic Pt−Sb core from potential cycling. HAADF-STEM images revealed that potential cycling on PtSb formed a 1 nm thick pseudomorphic Pt shell oriented along the [111] direction that covered the PtSb core. The differences in contrast between the brighter Pt shell and the darker PtSb core were caused by the differences in z contrast of the layers (Figure 2b). EDS line scans provided confirmation that the bright shell was composed of Pt (Figure S4). The (011) planes of the Pt shell had a d spacing of 2.4 Å, which was ~10% smaller than the equilibrium d spacing of 2.65 Å. HAADF-STEM images revealed that potential cycling of $PtSb_2$ formed a 1 nm thick pseudomorphic Pt shell oriented along the [100] direction that covered the $PtSb_2$ core (Figure 2c). The (002) planes of the Pt shell had a d spacing of 2.2 Å, which was ~4% larger than the equilibrium d spacing of 1.95 Å. Taken together, CV conditioning enriched the surface of the Pt−Sb nanoparticles with Pt, resulting in a shell that contained 10% compressive strain and 4% tensile strain for PtSb@Pt and $PtSb_2$@Pt, respectively.

The HOR performance was measured by collecting linear sweep voltammograms (LSVs) on a rotating-disk electrode (RDE) at a 5 mV s^{-1} scan rate (Figure 3a). The HOR performance of the Pt−Sb@Pt materials was compared to carbon-supported Pt nanoparticles which served as a benchmark. The half-wave potential ($E_{1/2}$) of PtSb@Pt was 0.041 V, which was 17.9 mV lower than that of Pt ($E_{1/2}$ = 0.059 V) and 28 mV lower than that of $PtSb_2$@Pt ($E_{1/2}$ = 0.069 V), demonstrating that PtSb@Pt exhibited superior activity on a geometric-area-normalized basis. The exchange current density, j_{oPt}, was calculated from the Butler−Volmer equation and normalized by the electrochemically active surface area of Pt on the electrode (Figure 3b and Figure S7).[37,38] PtSb@Pt displayed a j_{oPt} value of 0.9 mA cm^{-2}, which was ~1.6× larger

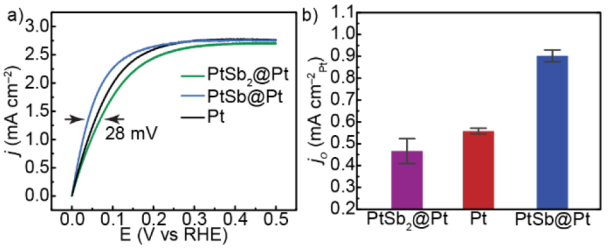

Figure 3. Hydrogen oxidation performance of Pt, PtSb@Pt, and $PtSb_2$@Pt measured by (a) linear sweep voltammetry normalized by the geometrical area on a rotating-disk electrode at 1600 rpm and a sweep rate of 5 mV s^{-1}, and (b) the mass-transport-corrected exchange current density (j_o) normalized by the electrochemically active surface area on a Pt basis.

than that of Pt (j_{oPt} = 0.56 mA cm^{-2}) and ~2× larger than that of $PtSb_2$ (j_{oPt} = 0.46 mA cm^{-2}) (Figure 3a). To provide insight into the mechanism of the HOR on the surface-modified ordered intermetallic Pt−Sb materials, we calculated the Tafel slopes from the mass-transport-corrected quasi-steady-state LSVs (Figure S8). All of the Pt−Sb materials and Pt exhibited Tafel slopes near 120 mV dec^{-1}, which is consistent with a mechanism involving a rate-determining one-electron-transfer step.[42−44] A 120 mV dec^{-1} Tafel slope can occur for several different rate-limiting steps for the HOR and depends on the surface coverage of adsorbed H; therefore, we cannot assign a specific rate-determining step solely by the Tafel slope.[45] Taken together, surface-modified PtSb was found to exhibit the highest j_{oPt} value, indicating that it possessed superior HOR activity at equilibrium relative to Pt and $PtSb_2$.

To provide mechanistic understanding into why PtSb@Pt exhibited superior HOR activity relative to Pt and $PtSb_2$@Pt phases, we interrogated the electronic structure of the materials via X-ray photoelectron spectroscopy (XPS) valence band spectroscopy to quantify the valence band center (ε_d) of the materials (Figure 4 and Figure S9). The electronic structure of a material controls the ε_d value (i.e., d-band center) of a material which is linked to the adsorption energy of reaction intermediates.[46,47] Alloying Pt with Sb causes d−p orbital hybridization via the ligand effect, downshifting the ε_d values of PtSb (2.91 eV) and $PtSb_2$ (3.25 eV) relative to that of Pt (2.87 eV). A downshifted ε_d relative to the Fermi level suggested that the adsorption energy of key reaction intermediates was weaker for both Pt−Sb intermetallics than for Pt. However, potential cycling of the Pt−Sb intermetallics created a Pt shell over the intermetallic core which is the active site that mediates HOR. Pt shells with thicknesses greater than two atomic layers are too thick to exhibit changes in adsorption energy from the ligand effect.[48−53] Therefore, strain is the

https://doi.org/10.1021/acsenergylett.2c02473
ACS Energy Lett. 2023, 8, 685−690

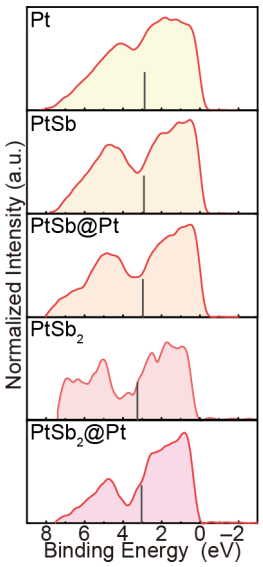

Figure 4. (a) X-ray photoelectron spectroscopy (XPS) valence band spectra. The gray vertical lines designate the valence band center (ε_d). The Fermi level is at 0 eV.

critical parameter which dictates the adsorption energy of the Pt shells over Pt−Sb intermetallics. To reveal insights into the role of strain, we interrogated the shift of the ε_d values between the Pt−Sb intermetallics and the Pt−Sb@Pt core−shell materials. The ε_d value of PtSb@Pt was 2.97 eV, which shifted 0.06 eV away from the E_f value relative to pristine PtSb (Figure 4). Thus, we can conclude that the 10% compressive strain of the Pt shell on PtSb@Pt serves to reduce the adsorption energy of reaction intermediates, resulting in improved HOR performance. In contrast, the ε_d value of $PtSb_2$@Pt was 3.04 eV, which shifted 0.21 eV upward toward the E_f value relative to PtSb (Figure 4). Therefore, the 4% tensile strain of the Pt shell on $PtSb_2$@Pt resulted in an increase in the adsorption energy of reaction intermediates, which is unfavorable. The overall ε_d value of $PtSb_2$@Pt was still lower than that of Pt because the $PtSb_2$ core of the particles contributes to the signal of the valence band spectra. Furthermore, changes of the ε_d values as a function of strain may not move linearly with the strain field.[54] It is also worth noting that XPS valence measurements are collected on powders which cover several hundred particles; these results validate that the compressive or tensile strain fields measured by TEM occurred on a global scale. Taken together, these results demonstrate that compressive strain on PtSb@Pt reduces the HBE, resulting in increased HOR performance, while tensile strain on $PtSb_2$@Pt increases the HBE and lowers the HOR performance.

To provide insight into the changes of the surface coverage of OH_{ads} on Pt and Pt−Sb@Pt, we evaluated the electro-oxidation of surface adsorbed CO. The rate of this reaction is determined by both the surface coverages of CO_{ads} and OH_{ads} and the probability of interaction of these two coadsorbed species (eq 4).[3,16,55]

$$CO_{ads} + OH_{ads} + OH^- \rightarrow CO_2 + e^- + H_2O \quad (4)$$

The onset for the electro-oxidation the CO adlayer was ∼0.2 V for $PtSb_2$@Pt, 0.25 V for PtSb@Pt, and 0.4 V for Pt (Figure S7). Therefore, the oxophilicity of the Pt sites on the surface had the following order: $PtSb_2$@Pt > PtSb@Pt > Pt. Interestingly, we do not observe a meaningful trend between the HOR activity and the CO oxidation onset, suggesting that OH_{ads} is not a promoter on pure Pt surfaces.

In summary, ordered intermetallic PtSb and $PtSb_2$ nanoparticles with Pt shells were developed as catalysts for the alkaline HOR. Potential cycling formed Pt shells over the Pt−Sb intermetallic, resulting in strained Pt overlayers. This strategy offers a unique advantage to solid-solution alloys because the strain field of Pt shells can be tuned in either direction, relative to elemental Pt, by altering the crystal structure of the intermetallic core, despite the materials being composed of the same two elements. PtSb@Pt was found to exhibit a superior electrocatalytic performance for the HOR, outperforming Pt and $PtSb_2$@Pt by over 1.6× and 2×, respectively, on a specific activity basis. The Pt shells on PtSb@Pt exhibited 10% compressive strain and the Pt shells on $PtSb_2$@Pt exhibited 4% tensile strain because of differences in the crystal structures of the Pt−Sb cores. An analysis of the valence band center measured by XPS confirmed that the compressive strain of PtSb@Pt exhibited a downshifted valence-band center relative to PtSb, which indicates that the HBE was lowered toward a more favorable energy for the HOR. In contrast, we found that tensile strain caused an upshift of the valence-band center related to $PtSb_2$, which indicates that HBE increased, which is unfavorable for the HOR. We also found that the surface coverage of adsorbed OH_{ads} does not appear to correlate with the strain field, suggesting that OH_{ads} is a spectator species. PtSb@Pt exhibits superior activity and lower cost than state-of-the-art Pt−Ru alloys that have been reported in the literature. PtSb@Pt is lower in cost than Pt, indicating that it is a promising material for alkaline fuel cell applications.

■ ASSOCIATED CONTENT

Supporting Information

The Supporting Information is available free of charge at https://pubs.acs.org/doi/10.1021/acsenergylett.2c02473.

Representative TEM images of PtSb, $PtSb_2$, PtSb@Pt, and PtSb2@Pt nanoparticles, mass-transport-corrected Tafel plots of Pt, PtSb@Pt, and $PtSb_2$@Pt, CO stripping voltammograms for Pt, PtSb@Pt, and $PtSb_2$@Pt, and unsmoothed XPS valence band spectra of Pt, PtSb@Pt, and $PtSb_2$@Pt (PDF)

■ AUTHOR INFORMATION

Corresponding Authors

David Raciti − *Material Measurement Laboratory, National Institute of Standards and Technology (NIST), Gaithersburg, Maryland 20899, United States;* orcid.org/0000-0002-9580-4524; Email: david.raciti@nist.gov

Anthony Shoji Hall − *Department of Materials Science and Engineering, Johns Hopkins University, Baltimore, Maryland 21218, United States;* orcid.org/0000-0003-4134-4160; Email: shoji@jhu.edu

Authors

Tianyao Gong − *Department of Materials Science and Engineering, Johns Hopkins University, Baltimore, Maryland 21218, United States*

Hamdan Alghamdi − *Department of Chemical and Biomolecular Engineering, Johns Hopkins University, Baltimore, Maryland 21218, United States; STC-K Intermediate Catalysis MEA, SABIC Technology Center at*

https://doi.org/10.1021/acsenergylett.2c02473
ACS Energy Lett. 2023, 8, 685−690

King Abdullah University of Science and Technology, Thuwal 23955, Kingdom of Saudi Arabia

Complete contact information is available at: https://pubs.acs.org/10.1021/acsenergylett.2c02473

Author Contributions

T.G. and H.A. are cofirst authors.

Notes

The authors declare no competing financial interest.

■ ACKNOWLEDGMENTS

We gratefully thank the McQueen Lab and PARADIM at Johns Hopkins University for assistance with the XRD measurements, University of Maryland, Baltimore County, for assistance with ICP-MS measurements. We also thank Wei-Chang D. Yang and Aaron Johnston-Peck for guidance and instruction pertaining to HAADF-STEM acquisition and QSTEM simulations. A.S.H. acknowledges financial support from the National Science Foundation under award no. DMR-2047019.

■ REFERENCES

(1) Campos-Roldán, C. A.; Alonso-Vante, N. The Hydrogen Oxidation Reaction in Alkaline Medium: An Overview. *Electrochemical Energy Reviews* **2019**, *2* (2), 312−331.
(2) Sheng, W.; Gasteiger, H. A.; Shao-Horn, Y. Hydrogen Oxidation and Evolution Reaction Kinetics on Platinum: Acid vs Alkaline Electrolytes. *J. Electrochem. Soc.* **2010**, *157* (11), B1529.
(3) Zheng, J.; Sheng, W.; Zhuang, Z.; Xu, B.; Yan, Y. Universal dependence of hydrogen oxidation and evolution reaction activity of platinum-group metals on pH and hydrogen binding energy. *Science Advances* **2016**, *2* (3), e1501602.
(4) Yao, Z.-C.; Tang, T.; Jiang, Z.; Wang, L.; Hu, J.-S.; Wan, L.-J. Electrocatalytic Hydrogen Oxidation in Alkaline Media: From Mechanistic Insights to Catalyst Design. *ACS Nano* **2022**, *16* (4), 5153−5183.
(5) Omasta, T. J.; Zhang, Y.; Park, A. M.; Peng, X.; Pivovar, B.; Varcoe, J. R.; Mustain, W. E. Strategies for Reducing the PGM Loading in High Power AEMFC Anodes. *J. Electrochem. Soc.* **2018**, *165* (9), F710−F717.
(6) Ramaswamy, N.; Ghoshal, S.; Bates, M. K.; Jia, Q.; Li, J.; Mukerjee, S. Hydrogen oxidation reaction in alkaline media: Relationship between electrocatalysis and electrochemical double-layer structure. *Nano Energy* **2017**, *41*, 765−771.
(7) Gülzow, E. Alkaline fuel cells: a critical view. *J. Power Sources* **1996**, *61* (1), 99−104.
(8) Vogel, W.; Lundquist, L.; Ross, P.; Stonehart, P. Reaction pathways and poisons—II: The rate controlling step for electrochemical oxidation of hydrogen on Pt in acid and poisoning of the reaction by CO. *Electrochim. Acta* **1975**, *20* (1), 79−93.
(9) Strmcnik, D.; Uchimura, M.; Wang, C.; Subbaraman, R.; Danilovic, N.; van der Vliet, D.; Paulikas, A. P.; Stamenkovic, V. R.; Markovic, N. M. Improving the hydrogen oxidation reaction rate by promotion of hydroxyl adsorption. *Nat. Chem.* **2013**, *5* (4), 300−306.
(10) Qiu, Y.; Xin, L.; Li, Y.; McCrum, I. T.; Guo, F.; Ma, T.; Ren, Y.; Liu, Q.; Zhou, L.; Gu, S.; Janik, M. J.; Li, W. BCC-Phased PdCu Alloy as a Highly Active Electrocatalyst for Hydrogen Oxidation in Alkaline Electrolytes. *J. Am. Chem. Soc.* **2018**, *140* (48), 16580−16588.
(11) Lu, S.; Zhuang, Z. Investigating the Influences of the Adsorbed Species on Catalytic Activity for Hydrogen Oxidation Reaction in Alkaline Electrolyte. *J. Am. Chem. Soc.* **2017**, *139* (14), 5156−5163.
(12) Hu, J.; Kuttiyiel, K. A.; Sasaki, K.; Zhang, C.; Adzic, R. R. Determination of Hydrogen Oxidation Reaction Mechanism Based on Pt−Had Energetics in Alkaline Electrolyte. *J. Electrochem. Soc.* **2018**, *165* (15), J3355−J3362.
(13) Wang, H.; Abruña, H. D. IrPdRu/C as H2 Oxidation Catalysts for Alkaline Fuel Cells. *J. Am. Chem. Soc.* **2017**, *139* (20), 6807−6810.
(14) Wang, H.; Abruña, H. D. Rh and Rh Alloy Nanoparticles as Highly Active H2 Oxidation Catalysts for Alkaline Fuel Cells. *ACS Catal.* **2019**, *9* (6), 5057−5062.
(15) Wang, H.; Yang, Y.; DiSalvo, F. J.; Abruña, H. D. Multifunctional Electrocatalysts: Ru−M (M = Co, Ni, Fe) for Alkaline Fuel Cells and Electrolyzers. *ACS Catal.* **2020**, *10* (8), 4608−4616.
(16) Liu, E.; Jiao, L.; Li, J.; Stracensky, T.; Sun, Q.; Mukerjee, S.; Jia, Q. Interfacial water shuffling the intermediates of hydrogen oxidation and evolution reactions in aqueous media. *Energy Environ. Sci.* **2020**, *13* (9), 3064−3074.
(17) Liu, E.; Li, J.; Jiao, L.; Doan, H. T. T.; Liu, Z.; Zhao, Z.; Huang, Y.; Abraham, K. M.; Mukerjee, S.; Jia, Q. Unifying the Hydrogen Evolution and Oxidation Reactions Kinetics in Base by Identifying the Catalytic Roles of Hydroxyl-Water-Cation Adducts. *J. Am. Chem. Soc.* **2019**, *141* (7), 3232−3239.
(18) Wang, D.; Xin, H. L.; Hovden, R.; Wang, H.; Yu, Y.; Muller, D. A.; DiSalvo, F. J.; Abruña, H. D. Structurally ordered intermetallic platinum−cobalt core−shell nanoparticles with enhanced activity and stability as oxygen reduction electrocatalysts. *Nat. Mater.* **2013**, *12* (1), 81−87.
(19) Kim, C.; Dionigi, F.; Beermann, V.; Wang, X.; Möller, T.; Strasser, P. Alloy Nanocatalysts for the Electrochemical Oxygen Reduction (ORR) and the Direct Electrochemical Carbon Dioxide Reduction Reaction (CO2RR). *Adv. Mater.* **2019**, *31* (31), 1805617.
(20) Wang, Y.; Sun, D.; Wang, M.; Feng, Z.; Hall, A. S. Oxygen Reduction Electrocatalysis on Ordered Intermetallic Pd−Bi Electrodes Is Enhanced by a Low Coverage of Spectator Species. *J. Phys. Chem. C* **2020**, *124* (9), 5220−5224.
(21) Jacob, K. T.; Raj, S.; Rannesh, L. Vegard's law: a fundamental relation or an approximation? *International Journal of Materials Research* **2007**, *98* (9), 776−779.
(22) Yan, Y.; Du, J. S.; Gilroy, K. D.; Yang, D.; Xia, Y.; Zhang, H. Intermetallic Nanocrystals: Syntheses and Catalytic Applications. *Adv. Mater.* **2017**, *29* (14), 1605997.
(23) Wang, Y.; Hall, A. S. Pulsed Electrodeposition of Metastable Pd31Bi12 Nanoparticles for Oxygen Reduction Electrocatalysis. *ACS Energy Letters* **2020**, *5* (1), 17−22.
(24) Wang, Y.; Sun, D.; Chowdhury, T.; Wagner, J. S.; Kempa, T. J.; Hall, A. S. Rapid Room-Temperature Synthesis of a Metastable Ordered Intermetallic Electrocatalyst. *J. Am. Chem. Soc.* **2019**, *141* (6), 2342−2347.
(25) Yang, Y.; Xiao, W.; Feng, X.; Xiong, Y.; Gong, M.; Shen, T.; Lu, Y.; Abruña, H. D.; Wang, D. Golden Palladium Zinc Ordered Intermetallics as Oxygen Reduction Electrocatalysts. *ACS Nano* **2019**, *13* (5), 5968−5974.
(26) Sarkar, S.; Jana, R.; Suchitra; Waghmare, U. V.; Kuppan, B.; Sampath, S.; Peter, S. C. Ordered Pd2Ge Intermetallic Nanoparticles as Highly Efficient and Robust Catalyst for Ethanol Oxidation. *Chem. Mater.* **2015**, *27* (21), 7459−7467.
(27) Kuttiyiel, K. A.; Sasaki, K.; Su, D.; Wu, L.; Zhu, Y.; Adzic, R. R. Gold-promoted structurally ordered intermetallic palladium cobalt nanoparticles for the oxygen reduction reaction. *Nat. Commun.* **2014**, *5* (1), 5185.
(28) Matsumoto, F.; Roychowdhury, C.; DiSalvo, F. J.; Abruña, H. D. Electrocatalytic Activity of Ordered Intermetallic PtPb Nanoparticles Prepared by Borohydride Reduction toward Formic Acid Oxidation. *J. Electrochem. Soc.* **2008**, *155* (2), B148−B154.
(29) Rodrigues da Silva, M.; Ângelo, A. C. D. Synthesis and Characterization of Ordered Intermetallic Nanostructured PtSn/C and PtSb/C and Evaluation as Electrodes for Alcohol Oxidation. *Electrocatalysis* **2010**, *1* (2), 95−103.
(30) Bu, L.; Zhang, N.; Guo, S.; Zhang, X.; Li, J.; Yao, J.; Wu, T.; Lu, G.; Ma, J.-Y.; Su, D.; Huang, X. Biaxially strained PtPb/Pt core/shell nanoplate boosts oxygen reduction catalysis. *Science* **2016**, *354* (6318), 1410−1414.

(31) Wang, C.; Chen, D. P.; Sang, X.; Unocic, R. R.; Skrabalak, S. E. Size-Dependent Disorder−Order Transformation in the Synthesis of Monodisperse Intermetallic PdCu Nanocatalysts. *ACS Nano* **2016**, *10* (6), 6345−6353.
(32) Li, J.; Sun, S. Intermetallic Nanoparticles: Synthetic Control and Their Enhanced Electrocatalysis. *Acc. Chem. Res.* **2019**, *52* (7), 2015−2025.
(33) Xiao, W.; Lei, W.; Wang, J.; Gao, G.; Zhao, T.; Cordeiro, M. A. L.; Lin, R.; Gong, M.; Guo, X.; Stavitski, E.; Xin, H. L.; Zhu, Y.; Wang, D. Tuning the electrocatalytic activity of Pt by structurally ordered PdFe/C for the hydrogen oxidation reaction in alkaline media. *Journal of Materials Chemistry A* **2018**, *6* (24), 11346−11352.
(34) Zhao, T.; Wang, G.; Gong, M.; Xiao, D.; Chen, Y.; Shen, T.; Lu, Y.; Zhang, J.; Xin, H.; Li, Q.; Wang, D. Self-Optimized Ligand Effect in L12-PtPdFe Intermetallic for Efficient and Stable Alkaline Hydrogen Oxidation Reaction. *ACS Catal.* **2020**, *10* (24), 15207−15216.
(35) Lee, C. R.; Kang, S. G. Electrochemical stability of Co−Mo intermetallic compound electrodes for hydrogen oxidation reaction in hot KOH solution. *J. Power Sources* **2000**, *87* (1), 64−68.
(36) Wang, Y.; Hall, A. S. Pulsed Electrodeposition of Metastable Pd31Bi12 Nanoparticles for Oxygen Reduction Electrocatalysis. *ACS Energy Letters* **2020**, *5* (1), 17−22.
(37) Wang, Y.; Hall, A. S. Room-Temperature Synthesis of Intermetallic Cu−Zn by an Electrochemically Induced Phase Transformation. *Chem. Mater.* **2021**, *33* (18), 7309−7314.
(38) Sun, D.; Wang, Y.; Livi, K. J. T.; Wang, C.; Luo, R.; Zhang, Z.; Alghamdi, H.; Li, C.; An, F.; Gaskey, B.; Mueller, T.; Hall, A. S. Ordered Intermetallic Pd3 Bi Prepared by an Electrochemically Induced Phase Transformation for Oxygen Reduction Electrocatalysis. *ACS Nano* **2019**, *13* (9), 10818−10825.
(39) Li, X.; Chen, Q.; McCue, I.; Snyder, J.; Crozier, P.; Erlebacher, J.; Sieradzki, K. Dealloying of Noble-Metal Alloy Nanoparticles. *Nano Lett.* **2014**, *14* (5), 2569−2577.
(40) McCue, I.; Benn, E.; Gaskey, B.; Erlebacher, J. Dealloying and Dealloyed Materials. *Annu. Rev. Mater. Res.* **2016**, *46* (1), 263−286.
(41) Gan, L.; Heggen, M.; Rudi, S.; Strasser, P. Core−Shell Compositional Fine Structures of Dealloyed PtxNi1−x Nanoparticles and Their Impact on Oxygen Reduction Catalysis. *Nano Lett.* **2012**, *12* (10), 5423−5430.
(42) Fletcher, S. Tafel slopes from first principles. *J. Solid State Electrochem.* **2009**, *13* (4), 537−549.
(43) Tafel, J. Über die Polarisation bei kathodischer Wasserstoffentwicklung. *Zeitschrift für Physikalische Chemie* **1905**, *50U* (1), 641−712.
(44) Parsons, R. General equations for the kinetics of electrode processes. *Trans. Faraday Soc.* **1951**, *47* (0), 1332−1344.
(45) Shinagawa, T.; Garcia-Esparza, A. T.; Takanabe, K. Insight on Tafel slopes from a microkinetic analysis of aqueous electrocatalysis for energy conversion. *Sci. Rep.* **2015**, *5* (1), 13801.
(46) Hammer, B.; Nørskov, J. K. Theoretical surface science and catalysis-calculations and concepts. *Adv. Catal.* **2000**, *45*, 71−129.
(47) Nørskov, J. K.; Abild-Pedersen, F.; Studt, F.; Bligaard, T. Density functional theory in surface chemistry and catalysis. *Proc. Natl. Acad. Sci. U. S. A.* **2011**, *108* (3), 937−943.
(48) Zhang, X.; Lu, G. Computational Design of Core/Shell Nanoparticles for Oxygen Reduction Reactions. *J. Phys. Chem. Lett.* **2014**, *5* (2), 292−297.
(49) Moseley, P.; Curtin, W. A. Computational Design of Strain in Core−Shell Nanoparticles for Optimizing Catalytic Activity. *Nano Lett.* **2015**, *15* (6), 4089−4095.
(50) Adit Maark, T.; Nanda, B. R. K. Enhancing CO2 Electroreduction by Tailoring Strain and Ligand Effects in Bimetallic Copper−Rhodium and Copper−Nickel Heterostructures. *J. Phys. Chem. C* **2017**, *121* (8), 4496−4504.
(51) Adit Maark, T.; Peterson, A. A. Understanding Strain and Ligand Effects in Hydrogen Evolution over Pd(111) Surfaces. *J. Phys. Chem. C* **2014**, *118* (8), 4275−4281.
(52) Kitchin, J. R.; Nørskov, J. K.; Barteau, M. A.; Chen, J. G. Role of Strain and Ligand Effects in the Modification of the Electronic and Chemical Properties of Bimetallic Surfaces. *Phys. Rev. Lett.* **2004**, *93* (15), 156801.
(53) Stephens, I. E. L.; Bondarenko, A. S.; Grønbjerg, U.; Rossmeisl, J.; Chorkendorff, I. Understanding the electrocatalysis of oxygen reduction on platinum and its alloys. *Energy Environ. Sci.* **2012**, *5* (5), 6744−6762.
(54) Zheng, X.; Li, L.; Li, J.; Wei, Z. Intrinsic effects of strain on low-index surfaces of platinum: roles of the five 5d orbitals. *Phys. Chem. Chem. Phys.* **2019**, *21* (6), 3242−3249.
(55) Blizanac, B. B.; Lucas, C. A.; Gallagher, M. E.; Arenz, M.; Ross, P. N.; Marković, N. M. Anion Adsorption, CO Oxidation, and Oxygen Reduction Reaction on a Au(100) Surface: The pH Effect. *J. Phys. Chem. B* **2004**, *108* (2), 625−634.

https://doi.org/10.1021/acsenergylett.2c02473
ACS Energy Lett. 2023, 8, 685−690